Short-time Oxidation of Cast γ/γ'-Ni–Cr–Al–Ta–Re Alloys at 1,000 °C

K. Fritscher · O. Schubert · C. Leyens · U. Schulz

Abstract Cast Ni–Cr–Al base alloys with two Cr ranges, 7–9.5 at.% and 3–4 at.%, respectively, and with Re + Ta refractory element contents of up to 7.5 at.% were subjected to oxidation experiments in air. The oxidation conditions were 100 h continuously at 1,000 °C and discontinuously for 500 h at temperature by cycling between room temperature and 1,000 °C. The times at temperature to the onset of scale spallation were monitored. Scale formation was investigated by SEM, EDS and XRD. The thermal expansion of the alloys and the lattice parameter of their γ-Ni phases were determined to assess their effect on the oxidation performance. Scale adhesion appears to be affected by mechanical interlocking at the alloy/scale interface.

Keywords Cyclic oxidation · Thermally grown oxide scale · Internal oxide · Spallation · Ni–Cr–Al–Re–Ta alloys

Introduction

Improved materials performance in hostile environments at elevated temperatures is a mayor key for achieving higher efficiencies of energy conversion in gas turbine engines. Best suited are high temperature oxidation resistant cast single-crystal

K. Fritscher (✉) · U. Schulz
DLR German Aerospace Center, Institute of Materials Research, 51170 Cologne, Germany
e-mail: klaus.fritscher@goettersiedlung.de

O. Schubert
Department HAM WR 420, Lufthansa Technik AG, 22335 Hamburg, Germany

C. Leyens
Institut für Werkstoffwissenschaft, Technische Universität Dresden, 01062 Dresden, Germany

superalloys protected by thermal barrier systems, as is common in modern aircraft propulsion engines and progressively employed in industrial gas turbines [1].

The superior high temperature mechanical properties of superalloys are a result of the coherent combination of two fcc phases with close-to-zero misfit. They are the high strength γ'-Ni$_3$Al phase with a volume fraction of approximately 60–80 % distributed in a γ-Ni$_{ss}$ matrix. The addition of refractory elements (REs) such as W, Ta, Mo and Re to Ni-based alloys has increased the creep-resistance of cast single-crystal superalloys, which have enabled higher operating temperatures. The so-called 2nd generation superalloys contain roughly 6Al–7Cr–17RE (in wt%) with around 3 wt% being Re. A gain of about 30–35 °C in operating temperature compared to that of former generation single-crystal superalloys was observed [2]. In 3rd generation cast single-crystal superalloys the Al content is maintained at around 6 wt% while the total RE content is raised towards 20 wt% including 6 wt% rhenium ($\sim$2 at.% Re). This enabled a further gain in operation temperature by about 30 °C [2]. In the 3rd generation superalloys the increase in rhenium content is offset by decreasing the Cr content from about 7 wt% to between 2 and 4.5 wt%. In addition to superior mechanical properties the alloys exhibit good or fair high temperature oxidation resistance due to the formation of protective alumina scales [3].

Oxidation tests on 3rd generation SX alloys, however, have revealed phase instabilities. One of which is the occurrence of oxidation-induced phase transformations to topologically close-packed (TCP) σ phase, which are found to be precursors for an internal secondary reaction zone [4]. For example, at temperatures up to 1,000 °C a protective alumina scale may not form on a CMSX-10 3rd generation superalloy [5]. Instead, due to selective oxidation of nickel from the near-surface region, an external NiO scale forms first. The resultant increase in aluminum concentration in the alloy shifts the composition from that of the bulk ($\gamma + \gamma'$) two-phase field to the single-phase β-NiAl field. Inward diffusion of oxygen creates an internal zone of precipitates of predominantly NiTa$_2$O$_6$. Increasing the temperature to $\geq$1,000 °C caused a more rapid depletion of Ni and formation of δ (Al$_3$Ni$_2$) phase. This phase is subjected to internal oxidation of Al, and a diffusion-retardant line of internal alumina particles develops, and remarkably reduced oxidation rates result [5]. So the formation of δ may be an interesting alternative for alumina-forming coatings to control high temperature oxidation. But the stability range of the δ phase terminates at $\sim$1,130 °C [6]. So protective coatings will be mandatory for the use of advanced-generation single-crystal superalloys.

Most current overlay coatings, which are composed of the four elements Ni, Co, Cr and Al, do not contain RE; but the disparity in RE content between the coating and single crystal superalloy may be critical in terms of interdiffusion and successive long-term strength decay in the diffusion-affected zone, notably in the thin-walled sections of turbine blades.

This study will investigate the oxidation resistance of NiCrAl-based coating formulations that are alloyed with particular RE's, where Ta and Re show merit. Reactive elements (Y, Zr, Hf etc.) will be left out. The effect of Ta is reported to supplement the hot corrosion resistance of Cr containing alloys [7], and to be the

most critical element besides Al and Cr to impart cyclic oxidation resistance to Ni-base superalloys [8]. Attempts have been made to relate the favorable oxidation resistance of Ta-containing NiCoCrAlY coatings to stresses between coating and oxide scales that build up during oxidation [9].

A favorable effect of Re on the corrosion properties of superalloys has been reported [10, 11]. Re-containing overlay coatings have been successfully introduced into industrial gas turbines [11]. Re additions accelerate the $\theta \rightarrow \alpha$ phase transformation of alumina scales on the β-NiAl phase thus favoring a reduced oxidation rate during the first period of heat exposure [8]. A Re content between 0.25 and 2 at.% was found to be harmful for the oxidation resistance of Ni–Acr–2Ti–10Al alloys (in at.%); however it was favorable for this alloy family by increasing the Al content to 15 at.% Al [12]. This high Re content is also typical for 2nd and 3rd generation single crystal superalloys commonly containing $\sim$15 at.% ($\sim$6 wt%) Al.

Provided that the application of a pioneering composition for overlay coatings on superalloys is proposed there are several fundamental issues to consider [3]:

(1) There must be a good thermal expansion match between coating and substrate, otherwise degradation could occur.
(2) There must be a good chemical compatibility between the coating and substrate, otherwise undesirable metallic phases could form. Instability issues may be associated with the addition of higher levels of RE.
(3) From the mechanical properties standpoint, most oxidation-resistant coating compositions have relatively low high-temperature strength, and therefore can have problems with fatigue or deformation during service thus limiting their durability.
(4) Finally, there can be a long-term problem of interdiffusion between coating and substrate, particularly the loss of the protective scale-forming element to the substrate. This is an acute problem for the durability of NiPtAl diffusion coatings at high temperatures and their inferior creep resistance. Castings of a modified NiPtAl composition with γ–γ' phase structure have been studied. They showed a superior inherent propensity of this γ–γ' material class for rumpling on thermal cycling [13].

Referring to (1) good thermal expansion match:

Ternary Ni–Cr–Al alloys are subjected to a critical volume increase at 995–996 °C which is due to the invariant reaction (Ni) + β-NiAl $\leftrightarrow$ γ'-Ni$_3$Al + (Cr) at this temperature [14, 15]. This substantial rise is reduced by adding further elements (e.g. Co. Re and Ta) introduced in the experimental Ni–Cr–Al alloys.

Referring to (2): the so-called secondary reaction zone beneath the bond coat is critical as it reduces the load-bearing cross section of the thin-walled turbine airfoils. Coatings should be compositionally adapted to their substrates. This is intended by proper alloying with Re and Ta.

Referring to (3): The problems of low strength of typical β + γ phase overlay and β-phase diffusion bondcoats can be solved if appropriate γ/γ'-based coatings are taken which are solid-solution strengthened by alloying with Re and Ta.

Referring to (4): no interdiffusion is expected to run in "EQ coatings" which are designed to be thermodynamically in equilibrium with the substrate [16]. They represent a reasonable concept in cases where one of the two phases of the single crystal substrates—preferably the γ'-Ni$_3$(Al,Ta) phase—is highly oxidation-resistant and can be used as a coating formulation.

Potential γ–γ' bond coat compositions may be advantageous for the protection of 2nd and 3rd generation superalloys, as they provide the best possible motive to the four fundamental issues given above. So NiCrAl base γ–γ' compositions with Cr contents similar to the 2nd and 3rd generation superalloys will be alloyed with Ta and Re up to their saturation limits. To come close to the structural features characteristic for single crystal superalloys the ratio of the phases will be kept to 75 % of γ' phase and 25 % of Ni$_{ss}$. The presence of TCP and other phases is intended to be excluded. The absence of Co and a low Cr content allow for an extension of the limits of saturation with Ta and Re. In addition the shortfall of the critical invariant reaction at $\sim$995 °C as mentioned above will not occur in a quinary alloy system consisting of Ni, Cr, Al, Ta, and Re. The high content of Ta and Re in the experimental alloys is expected to reduce the overall diffusivity. Hence potential inter-diffusion between these alloys and the single-crystal substrates is rated low. As Ta will mainly solution-strengthen the γ' phase by forming γ'-Ni$_3$(Al,Ta) and Re the γ-Ni$_{ss}$ phase, the integral strength will be enhanced in both phases and will contribute to the overall strength of a component. Parasitic loading of turbine blades by their coatings can be reduced.

The oxidation behavior of NiCrAlTaRe alloy compositions will be investigated by isothermal and cyclic oxidation tests of substandard duration. Spallation resistance is here of prime interest for a potential bondcoat formulation in potential thermal barrier systems. The thermal expansion coefficient (CTE) of the alloys and the lattice parameters will be determined. Their effect on the performance of the alloys on heat exposure will be discussed.

Experimental Procedures

A proprietary software package PHASCALC (Forschungszentrum Juelich) was used to calculate the composition of thirteen γ/γ'-based Ni–Cr–Al–Ta–Re alloys. Two directives with priorities as follows were given to the software: (i) the ratio of γ to γ' phase to be held constant at 75 vol.% for γ' and 25 vol.% for γ. (ii) two ranges for chromium at $\sim$4 and $\sim$8 at.% which were ranked subordinate. The concentrations were computed by incremental iterations to approach the compositional target range for Cr.

The alloy compositions were prepared from high purity elemental materials. Electrolytic chromium flakes of a nominal sulfur content of 3 ppmw and nickel pellets of 2 ppmw were charged in alumina crucibles. Double-refined electrolytic Al and electron-beam refined droplets of Ta and Re were added. Cylindrical slabs were made by induction melting in vacuum (RF VIM) and casting into a rotating carousel copper mould. The slabs were of 16 mm diameter for the manufacture of samples for oxidation experiments and 5 mm diameter for thermal expansion measurements.

The flowability of some compositions was found to be problematic, as mushy sediments were sometimes observed as remnants at the bottom of the crucibles. In particular compositions containing more than 3 at.% Re were difficult to run which can be attributed to the extra-high Al concentrations necessary to stabilize 75 % of γ'-phase within the castings. Melts with high Ta contents turned out to be cast more easily. The quantity of off-evaporated elements and in particular of chromium was difficult to control, because unpredictable residence times for the liquefaction of the batches in vacuum were concerned. Hence the target compositions and those of the final castings were rather different at times, and the 1:3 ratio of γ to γ' phase was affected likewise.

The cast slabs were fitted into stainless steel tubes at either side sealed by electron-beam welding. They were hot-isostatically pressed under argon atmosphere at 1,250 °C for 4 h and 1,500 atm pressure to eliminate inherent casting porosity. Their chemical composition was determined by wave-length X-ray fluorescent analysis (XRF) as given in Tables 1 and 2. The portion of γ' in the castings was recalculated with respect to the XRF analyses and is given in Table 3. The occurrence of other phases than γ and γ' is noted there as well.

The slabs were spark-erosion cut to cylindrical coupons of 15 mm diameter and 1 mm thickness and mechanically finished with 800 grit emery. The coupons were fitted with a hole for suspending during furnace testing.

Thermocyclic tests on the coupons were run in air consisting of discontinuous 500 h oxidation comprising daily heating cycles at 1,000 °C for 22 h followed by 2 h cool down to RT and reheating. Isothermal oxidation tests were conducted at 1,000 °C for 100 h.

Thermal expansion measurements were conducted on the 5 mm diameter slabs of 50 mm length homogenization-annealed at 1,100 °C for 4 h. They are included in Table 3.

Scanning electron microscopy (SEM; GEMINI LEO 982) equipped with energy dispersive spectroscopy (EDS) was applied for examination and identification of the oxide phases thermally grown after 500 h cyclic exposure times at 1,000 °C. X-ray diffraction (XRD; Siemens 5000) was used to determine the phases present in the

Table 1 Composition of alloys having 7–9.5 at.% Cr (wt% given in *italics*)

Alloy designation	Ni	Cr	Al	Ta	Re
A	66.95	7.85	21.74	0.37	3.09
	70.6	*7.3*	*10.5*	*1.2*	*10.3*
B	71.31	6.94	18.19	1.10	2.46
	73.5	*6.3*	*8.6*	*3.5*	*8.0*
C	71.09	9.52	15.44	1.97	1.98
	71.8	*8.5*	*7.2*	*6.1*	*6.4*
D	70.83	8.53	15.00	2.76	2.88
	68.8	*7.3*	*6.7*	*8.3*	*8.9*
E	69.28	8.95	14.44	2.57	4.76
	64.8	*7.4*	*6.2*	*7.4*	*14.1*

Table 2 Composition of alloys having 3–4 at.% Cr (wt% given in *italics*)

Alloy designation	Ni	Cr	Al	Ta	Re
F	73.84	3.11	19.21	–	3.84
	75.7	*2.8*	*9.1*	*–*	*12.5*
G	70.91	3.40	22.91	1.11	1.67
	76.1	*3.2*	*11.3*	*3.7*	*5.7*
H	79.07	3.13	12.56	2.46	2.78
	76.0	*2.7*	*5.6*	*7.3*	*8.5*
I	75.77	3.55	13.98	3.72	2.98
	71.3	*3.0*	*6.1*	*10.8*	*8.9*
K	76.11	3.28	13.13	4.57	2.91
	70.2	*2.7*	*5.6*	*13.0*	*8.5*
L	75.07	3.73	12.92	4.63	3.65
	68.1	*3.0*	*5.4*	*13.0*	*10.5*
M	71.61	4.06	15.40	3.51	5.42
	64.9	*3.3*	*6.4*	*9.8*	*15.6*
N	76.63	4.21	12.47	6.69	–
	70.9	*4.3*	*5.4*	*19.4*	*–*

Table 3 Phases in the castings, γ' portion (calculated), lattice parameter of γ-Ni phase, lattice expansion of γ-phase by substitutional alloying with Re + Ta compared to pure γ-Ni (%), and thermal expansion between RT and 1000 °C (%)

Alloy	Crystal structures	γ'-Ni$_3$(Al,Ta) content, calculated (at.%)	Lattice parameter a of γ-Ni phase (nm)	$\Delta a/a_{lit}$ (%) for γ phase	Mean thermal expansion at 1000 °C (%)
A	(γ), γ', δ, σ-Re$_2$Cr	81.5	0.35745	1.436	1.506
B	(γ), γ', δ	79.9	0.35713	1.345	1.511
C	γ, γ'	73.4	0.35763	1.487	1.547
D	γ, γ', δ	74.5	0.35822	1.654	1.482
E	γ, γ', δ	63.8	0.35786	1.552	1.486
F	(γ), γ', δ	78.1	0.35606	1.041	1.549
G	γ, γ', δ	61.3	0.35758	1.473	1.451
H	γ, γ', δ	72.2	0.35795	1.578	1.475
I	γ, γ', δ	71.1	0.35831	1.680	1.423
K	γ, γ', δ	72.1	0.35841	1.708	1.408
L	γ, γ', δ	71.7	0.35844	1.717	1.384
M	γ, γ', δ	77.3	0.35776	1.524	1.416
N	γ, γ', η-NiTa	78.7	0.35883	1.828	1.396

cast alloys and to calculate the lattice parameter of the γ-Ni phase. The thermal expansion of the alloys was recorded during heating at a rate of 2 K/min in a high-vacuum dilatometer (Bähr).

Results

Scale Formation on Cast Alloy Coupons

Cross-sectional micrographs of the cast alloys (compositions in Table 1 and 2) after 500 h cyclic oxidation at 1,000 °C are presented in Figs. 1, 2, 3, 4, 5, 6, and 7. The near-surface γ-Ni/γ'-Ni$_3$(Al,Ta) microstructure of the alloy matrix is often intermingled with additional δ-Cr(Re) phases which are characteristic micron-sized bright rounded inclusions as is best seen in Fig. 3. Some physical details of the original matrix (lattice parameters of γ-Ni$_{ss}$, thermal expansion) and the γ/γ' ratio are given in Table 3.

The scales which have formed on the alloys are presented on the right of the micrographs. They all show a sublayer of alumina that is either continuous or case by case broken in a pearl chain like manner (e.g. see alloy N in Fig. 4). But exclusive alumina formation has never been observed. Instead spinel phases and NiO follow consecutively hereby forming layers or discontinuous patches. Ta$_2$O$_5$ phase may stay in between the layers. Below the alumina layer internal oxidation may have occurred thus forming intrusions, pegs and internal oxides in the metal matrix. The oxide phase arrangements observed in the various scales are summed up in Table 4.

Oxidation Kinetics

Cyclic Oxidation

On thermocyclic exposure (one cycle: 22 h at 1,000 °C, 2 h cool down to RT) the alloys containing 7–9.5 at.% Cr mostly exhibit a heavy weight increase with time
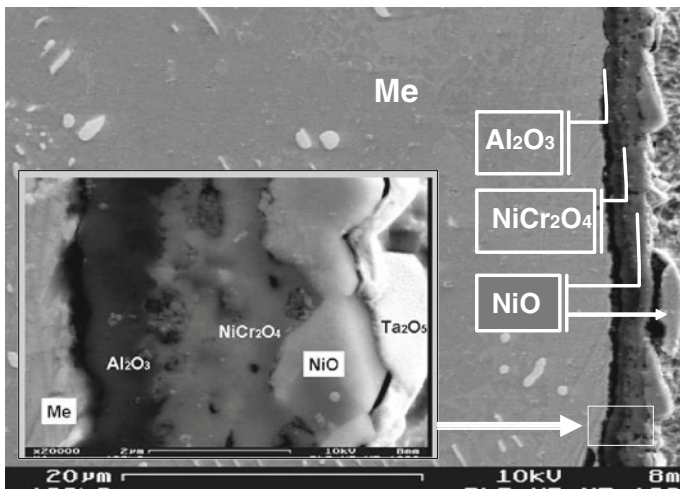

Fig. 1 SEM image of the Me/MeO interface cross section of alloy B taken from a site having a Ta$_2$O$_5$ top coating showing a continuous alumina layer of about 1 μm thickness (*black*) followed by about 2 μm thick porous NiCr$_2$O$_4$ spinel and coarse-grained NiO, covered by non-adherent Ta$_2$O$_5$ (*white*) containing traces of alumina. Casual NiO is on top
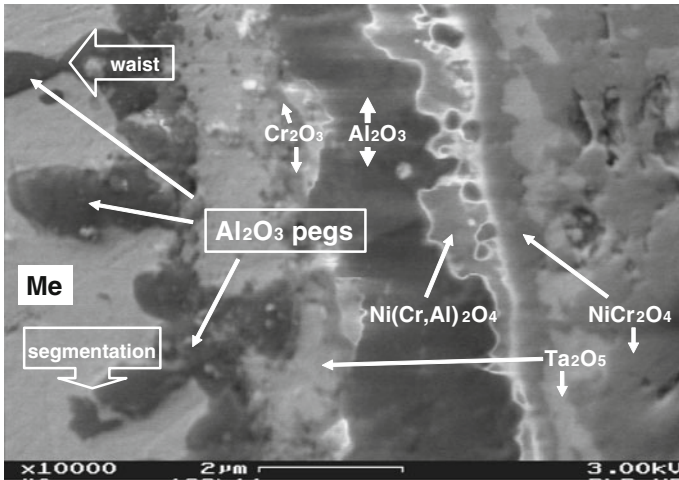
Fig. 2 Me/MeO interface area of alloy C showing a discontinuous alumina layer with protruding pegs followed by a irregular Ta_2O_5 layer and a chromia fringe followed by a continuous alumina layer and an Al-containing and Al-devoid $NiCr_2O_4$ spinel and Ta_2O_5 between $NiCr_2O_4$, and NiO on top
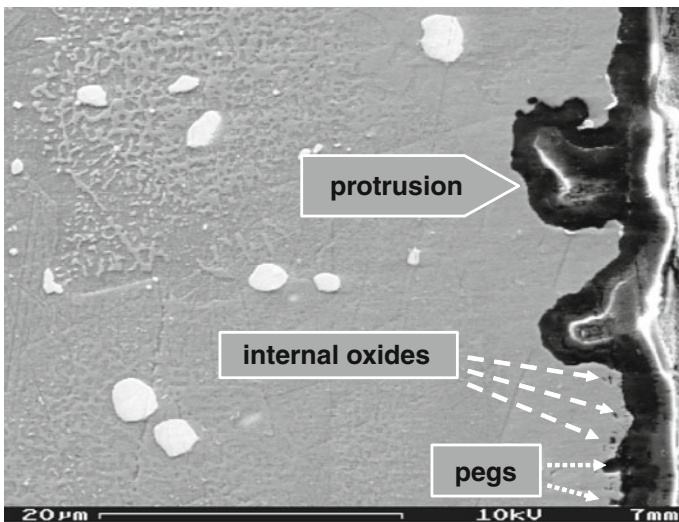

Fig. 3 Alloy M showing local internal oxides, alumina protrusions (~ 6 μm) interpenetrating the alloy, and up to 3 μm deep pegs. The scale consists of an $Al_2O_3/Ni(Cr,Al)_2O_4/NiO$ layer sequence. The substrate shows some δ-Cr(Re) particles (*bright*)

which calms down after the first cycle (see Fig. 3). The weight gain (weight loss for alloy B) is revitalized after ~ 3–4 cycles/~ 80–100 h). Arrows pointing to the weight change versus time graphs indicate the apparent onset of spallation of scales. The time without spallation is summarized in Table 5.
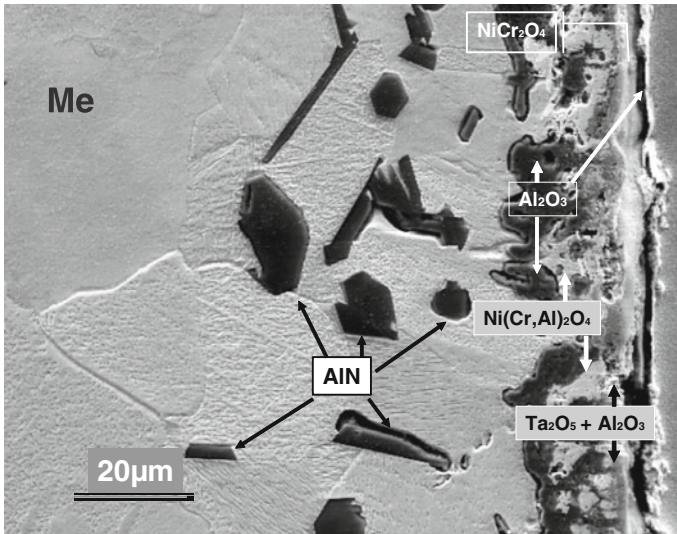
Fig. 4 Me/MeO interface of alloy N. The *inner* part shows AlN polygons (*black*) indicative of internal nitridation below a discontinuous and distorted alumina "layer" followed by a convoluted oxide arrangement of spinel phases, alumina and Ta_2O_5
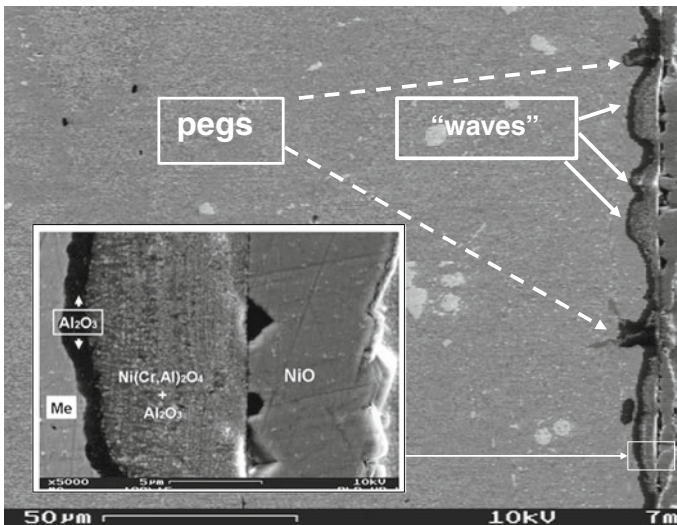

Fig. 5 Alloy K with a wavy Me/TGO interface and sporadic 7 μm deep alumina pegs anchoring in the metal at the depression between ≤8 μm "waves" shows a relatively thick and uneven scale of continuous layers of Al_2O_3, $Ni(Cr,Al)_2O_4 + Al_2O_3$ dispersal, and NiO. A similar scale arrangement is also with alloys F, G, H, I, L. K

On thermocyclic exposure of the alloys containing 3–4 at.% Cr they mostly show a steeply sloping initial weight gain in particular for alloys high in Re and Ta (e.g. alloys K, L and M, see Fig. 3). The oxidation kinetics of the three alloys changes abruptly in a slow oxidation mode, in the course of which no or late spallation is
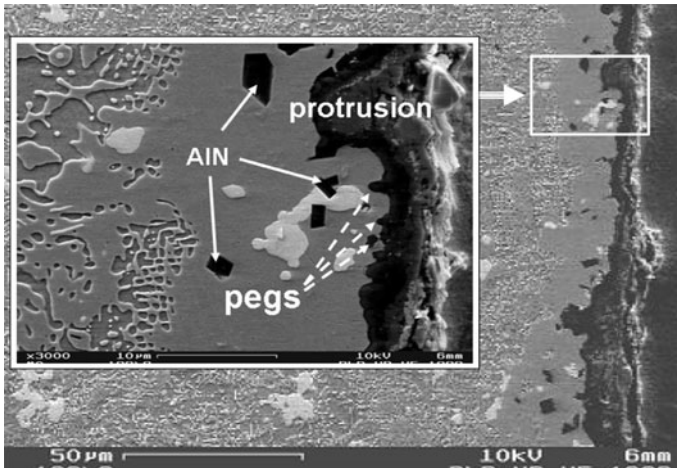
Fig. 6 Alloy "E" showing an irregular curled Me/TGO interface with sporadic ≤8 μm deep voluminous alumina protrusions with some spinel interior as well as slim 1–2 μm long alumina pegs. Internal oxides and AlN polygons spread close to the Me/TGO interface
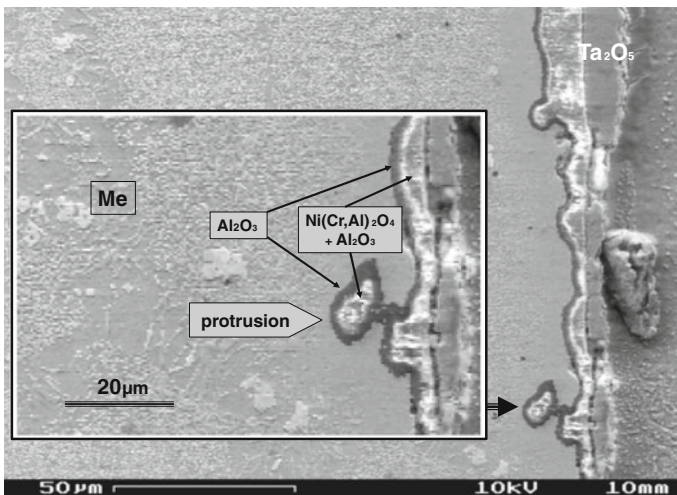

Fig. 7 Alloy "L" showing a relatively regular wavy alloy/alumina interface exhibiting sporadic up to 15 μm long mushroom-like protrusions filled up with internal spinels

observed. In contrast the alloys F, G, H and I start heavy spallation of sub-mm sized particles on cooling just after the first cycle (Fig. 8b).

Isothermal Oxidation

The weight gain rates on isothermal heat exposure at 1,000 °C are best approximated by the parabolic equation $\Delta m = m_0 + \sqrt{k_P}\sqrt{t}$ [17] (see Fig. 9a, b). m_0 and k_P are collated in Table 6. According to this equation three alloys containing

Table 4 Oxide phases consecutively identified on the alloys, intensity of internal attack by oxygen/ nitrogen, and times up to onset of spallation

Alloy designation	Typical oxide sequence on Ni–Cr–Al–Ta–Re alloys	Internal oxidation/ nitridation	Time to spallation observed
A	Al_2O_3/$NiCr_2O_4$/NiO	Nil	$\leq$88 h
B	Al_2O_3/$NiCr_2O_4$/NiO//Ta_2O_5 + Al_2O_3 dispersion//NiO[a]	Faint (local)	$\leq$88 h
C	Al_2O_3/Ta_2O_5/Cr_2O_3/Al_2O_3/$Ni(Cr,Al)_2O_4$/Ta_2O_5/ $NiCr_2O_4$	Moderate	$\leq$110 h[b]
D	Al_2O_3/$Ni(Cr,Al)_2O_4$/Ta_2O_5/$NiCr_2O_4$/NiO	Faint (local)	242 h
E	Al_2O_3/$Ni(Cr,Al)_2O_4$–$NiCr_2O_4$ + Ta_2O_5 dispersion/ $NiTaO_3$	Moderate	No spallation
F	Al_2O_3/$Ni(Cr,Al)_2O_4$ + Al_2O_3 dispersion//NiO[a]	Nil	$\leq$22 h
G	Al_2O_3/$Ni(Cr,Al)_2O_4$ + Al_2O_3 dispersion//NiO[a]	Nil	$\leq$22 h
H	Al_2O_3/$Ni(Cr,Al)_2O_4$ + Al_2O_3 dispersion//NiO[a]	Nil	22 h
I	Al_2O_3/$Ni(Cr,Al)_2O_4$ + Al_2O_3 dispersion//NiO[a]	Nil	$\leq$22 h
K	Al_2O_3/$Ni(Cr,Al)_2O_4$ + Al_2O_3 dispersion/Ta_2O_5//NiO[a]	Nil	No spallation
L	Al_2O_3/$Ni(Cr,Al)_2O_4$ + Al_2O_3 dispersion/Ta_2O_5//NiO[a]	Nil	198 h
M	Al_2O_3/$Ni(Cr,Al)_2O_4$/NiO	Faint (local)	352 h
N	Al_2O_3/$Ni(Cr,Al)_2O_4$/Al_2O_3 + Ta_2O_5 dispersion/ $NiCr_2O_4$/Ta_2O_5//NiO	Strong	88 h

[a] Double slash is indicating apparent de-cohesion between phases

[b] Spallation by predominant internal fracture through the oxide scale

Table 5 The times until onset of scale spallation from the alloys ranking from 100 h to $\geq$500 h set in a row to microstructural characteristics (pegs, protrusions) emerging at the Me/TGO interface

Alloy	Time to spallation in h (number of cycles in brackets)	Characteristic depth of oxide pegs/ protrusions	Distinctive type of oxide pegs/protrusions
C	110 (5)	2 μm	Multiple smooth pegs
L	198 (9)	15 μm	Sporadic rounded protrusions between smooth or waved interface sections
D	242 (11)	1–2 μm	Frequent smooth pegs
M	352 (16)	3 μm	Ragged pegs, sometimes of a dovetail type
E	$\geq$500 (>45)	1 μm pegs and 8 μm protrusions	Sporadic voluminous irregular protrusions and frequent needle-shaped pegs and waved interface sections
K	$\geq$500 (>45)	7 μm pegs and 8 μm wavy protrusions	Waved interface and irregular (dovetail-type) pegs at depressions between waves

7–9.5 at.% Cr (alloys B, C and E) exhibit low parabolic rate constants k_p between 3.5 and 6×10^{-8} mg^2 cm^{-4} s^{-1} (Fig. 9a). The low parabolic oxidation kinetics is starting after passing a transition period of about 20–30 h.

Four alloys containing 3–4 at.% Cr (alloys F, H, K, L) also exhibit relatively low parabolic rate constants k_p between about 7 and 10×10^{-8} mg^2 cm^{-4} s^{-1}, see
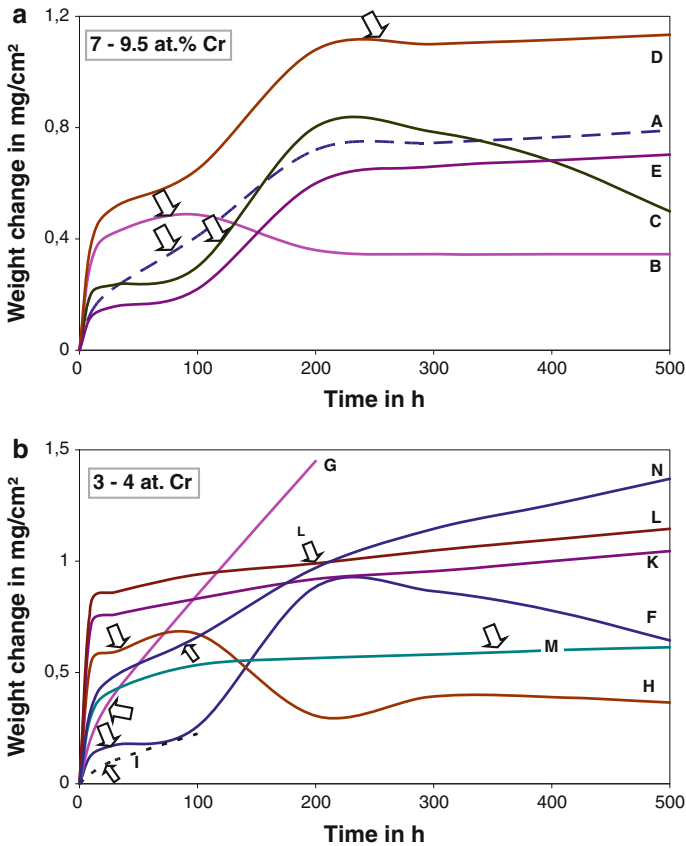
Fig. 8 a Weight change versus time of Ni–Cr–Al–Ta–Re alloys with 7–9.5 % Cr obtained on thermocyclic exposure (one cycle: 22 h at 1,000 °C, 2 h cool down to RT and reheating). *Arrows* indicate first observation of scale spallation. **b** Weight change versus time of Ni–Cr–Al–Ta–Re alloys with 3–4 % Cr obtained on thermocyclic exposure (one cycle: 22 h at 1,000 °C, 2 h cool down to RT and reheating). *Arrows* indicate first observation of scale spallation

Fig. 9b. For comparison the values are about twice as high as those for the associated alloys having 7 to 9.5 at.% Cr. The m_0 values are about three times higher on comparing the peak data (alloy K compared to alloy B, see Table 6). Nonetheless the transition periods of about 10 h are less than half the times compared to the related alloys with the higher Cr content thus indicating that the initial weight gain is extremely violent for the 3–4 at % Cr alloys.

Discussion

The oxidation and characterization of quinary NiCrAlReTa alloys represents an intermediate state of a route to the development of potential bondcoat compositions for advanced Ni-base single crystal superalloys. A superior compatibility between
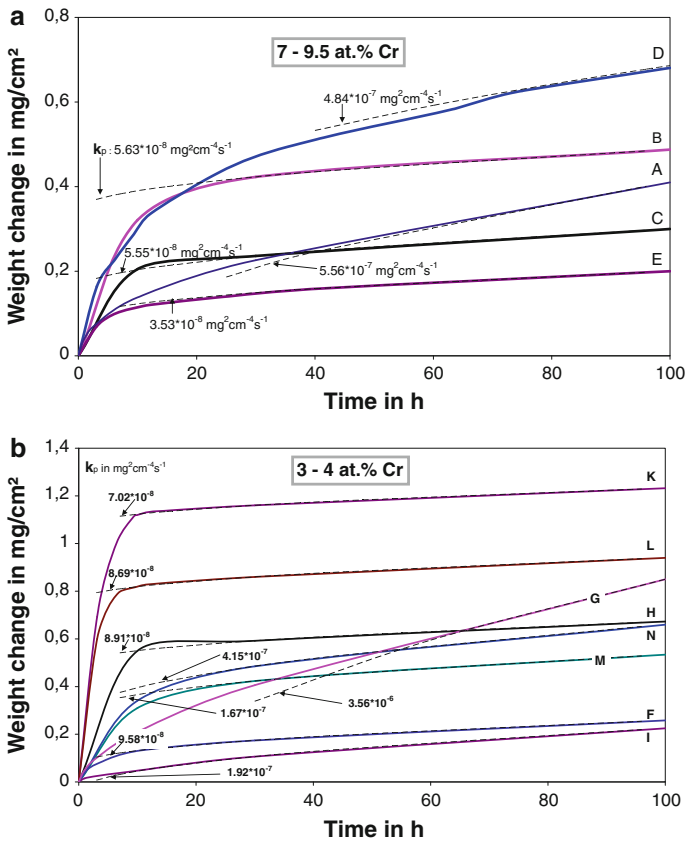
Fig. 9 a Weight gain versus time of Ni–Cr–Al–Ta–Re alloys with 7–9.5 % Cr on isothermal oxidation in air at 1,000 °C. **b** Weight gain versus time of Ni–Cr–Al–Ta–Re alloys with 3–4 % Cr on isothermal oxidation in air at 1,000 °C

superalloys and bondcoats is postulated via keeping comparable volume ratios of the γ/γ'-phases, and superior high-temperature mechanical properties are aimed at via solute-solution strengthening of the γ/γ'-phases with Re and Ta. Oxide maps will show the scales forming on the quinary alloys. A ranking between the oxidation behaviors may identify one or two compositions which are advisable to be optimized in successional studies by means of doping with reactive elements.

A roadmap for the best way of creating favorable coating compositions [3] was followed which covers four directives. The first three directives concern

(i) good chemical compatibility between the coating and substrate,
(ii) good high-temperature strength to avoid problems with fatigue or deformation
(iii) long-term stability against interdiffusion between coating and substrate.

Based on the above suggestions a careful examination was focused on a γ/γ' Ni-base alloy family which was backed up by substitutional solution strengthening with Re and Ta; this alloy class is closely related to advanced superalloys and is

Table 6 Parabolic fitting of experimental mass gain data by the equation $\Delta m = m_0 + \sqrt{k_p}\sqrt{t}$

Alloy	m_0 in mg $\times$ cm^{-2}	k_p in mg^2 cm^{-4} s^{-1}
A	−0.03756	5.56×10^{-7}
B	0.34489	5.63×10^{-8}
C	0.15849	5.55×10^{-8}
D	0.26880	4.84×10^{-7}
E	0.08724	3.53×10^{-8}
F	0.07227	9.58×10^{-8}
G	−0.28131	3.56×10^{-6}
H	0.49391	8.91×10^{-8}
I	−0.03811	1.92×10^{-7}
K	1.07281	7.02×10^{-8}
L	0.76312	8.69×10^{-8}
M	0.28858	1.67×10^{-7}
N	0.27307	4.15×10^{-7}

thought to meet all the above expectations. Special attention was concentrated on the last directive concerning (iv) a good thermal expansion match between metal substrate and coating. Here preference for low-expansion alloy compositions was given; they will aim at future potential low-expansion materials. They will have a good match to low-expansion ceramics e.g. protective thermal barrier coatings. Besides the expansion gap with α-alumina will become less as well. In this context Ta turns out to be more effective than Re in reducing the overall thermal expansion in the alloys, and is also more efficient than Re in expanding the lattice of the γ phase. The trend in creating a low TEC alloy by adding excessive Ta, however, may undermine the unimpeded formation of a protecting α-alumina scale as explained below.

The scales on the alloy buttons after 500 h cyclic oxidation at 1,000 °C in air are no exclusive alumina, but multi-layered scales instead. They commonly consisted of three-phase arrangements at least comprising alumina, spinel and NiO on top. Additional oxide phases often comprise varied spinel phases and tantalum oxides embedded in between those layers. Internal oxides and nitrides close to the alloy surface will be addressed below.

The weight gain kinetics during isothermal exposure at 1,000 °C could be mostly fitted by parabolae indicative for the diffusion-controlled action of protective scales during this period. Some of the low parabolic rate constants k_p compare well to the k_p data for alumina-forming alloys reported [18]. So the growth rate of multi-layer scales can apparently be controlled by the exclusive growth kinetics of the alumina subscale. Prior to that higher oxide growth rates were observed during a transition period of a few hours. Relatively high weight gains during this transient stage were measured especially for the low-chromium and high Ta + Re alloys. This very high initial weight gain is ascribed to the preferential oxidation of transition elements (mainly Ni), the restrained diffusivity of Al by Re and Ta, which both are hypothesized to be diffusion-impeding elements, and the reduced concentration of α-alumina-promoting Cr. Alternatively high weight gains by predominant formation of transient aluminas are supposed to be less likely.

Re additions are said to accelerate the $\theta \rightarrow \alpha$ phase transformation of alumina scales on β-NiAl phases [8]. The same influence on γ/γ' alloys cannot be excluded due to the following indication: the change in oxidation kinetics from a vigorous transient to a slow-going rather stringent parabolic growth mode is an instantaneous one. The $\theta \rightarrow \alpha$ phase transformation is over; otherwise parabolic kinetics would not have become established owing to the extremely high diffusion rates of transient alumina phases like the θ phase compared to the low one of stable α phase. For that reason phase transition in alumina sublayers during the "parabolic period" is unlikely.

The various alloys showed a distinctive oxidation behavior and scale adhesion. But some trends will be found out. So overcritical contents of Re and Ta, which are coexistent in the alloys, are needed to surpass a threshold of 100 h cyclic exposure at 1,000 °C without scale spallation. Figure 10a is representing the 7–9.5 at% Cr alloys: e.g. it shows superior adhesion of the scale (α-alumina, spinel, TaNiO$_3$) on alloy E of 500 h at least, thereby precipitating minor internal oxides and nitrides (given in Fig. 11a). Internal nitridation has also been reported for Ta-containing NiCoCrAlY coatings [19]. Obviously nitride formation is suppressed in the low-Cr quinary alloy variances. Besides the k_p rate constant during isothermal oxidation was outstandingly low. The two alloys of intermediate scale adhesion (C and D) had either six oxide phases, faint internal oxidation and an elevated k_p rate constant or slightly different oxide phases, medium internal oxidation and a low or intermediate k_p rate constant.

Similarly the oxidation behavior of the 3–4 at% Cr alloys is shown in Fig. 10b. This diagram displays superior adhesion of the scale (α-alumina, spinel, Ta$_2$O$_5$, NiO) on alloy K, showing no internal oxidation (Fig. 11b) and a low k_p rate constant during isothermal oxidation. Two vicinal alloys of intermediate scale adhesion (L and M) have quite the same oxide phases, no or faint internal oxidation and a low or intermediate k_p rate constant.

Figure 10a and b are tentative oxide maps. They link the alloy compositions of the quinary system Ni–Cr–Al–Ta–Re (for 7–9.5 % Cr in Fig. 10a, for 3–4 % Cr in Fig. 10b) as well to the oxide phases on the respective alloy compositions as to the estimated k_p rate constants and the time ranges with no scale spallaton. So some alloy buttons exhibit a reasonable but not excellent spallation resistance, although only intermediate k_p rate constants were realized. Minor internal oxides and nitrides near the metal/scale interface were also tolerated; they have no harmful effect.

Additionally the effect of the γ-Ni lattice spacing of the alloy matrix on oxidation behavior was considered; the γ-Ni lattice may fit to neighboring oxide layers thus influencing scale adhesion issues. A narrow epitaxial match between γ-Ni and α-alumina may be considered as seldom observed e.g. for a (113) α-Al$_2$O$_3$∥(111) γ-Ni relationship; an extant slight mismatch will lessen via increasing the γ-Ni lattice spacing [20]. No clear effect of the lattice spacing on oxidation and adhesion, however, could be discovered (respective graphs not shown here). Accordingly a dependency on lattice spacing seems unlikely.

The effect of *thermal expansion* of the alloys on oxidation was considered next. Cooling stresses between metal base and scales and successive spallation are considered to be definitely related to the thermal mismatch. This assumption was proved wrong. No dependency of spallation resistance during cyclic heat exposure
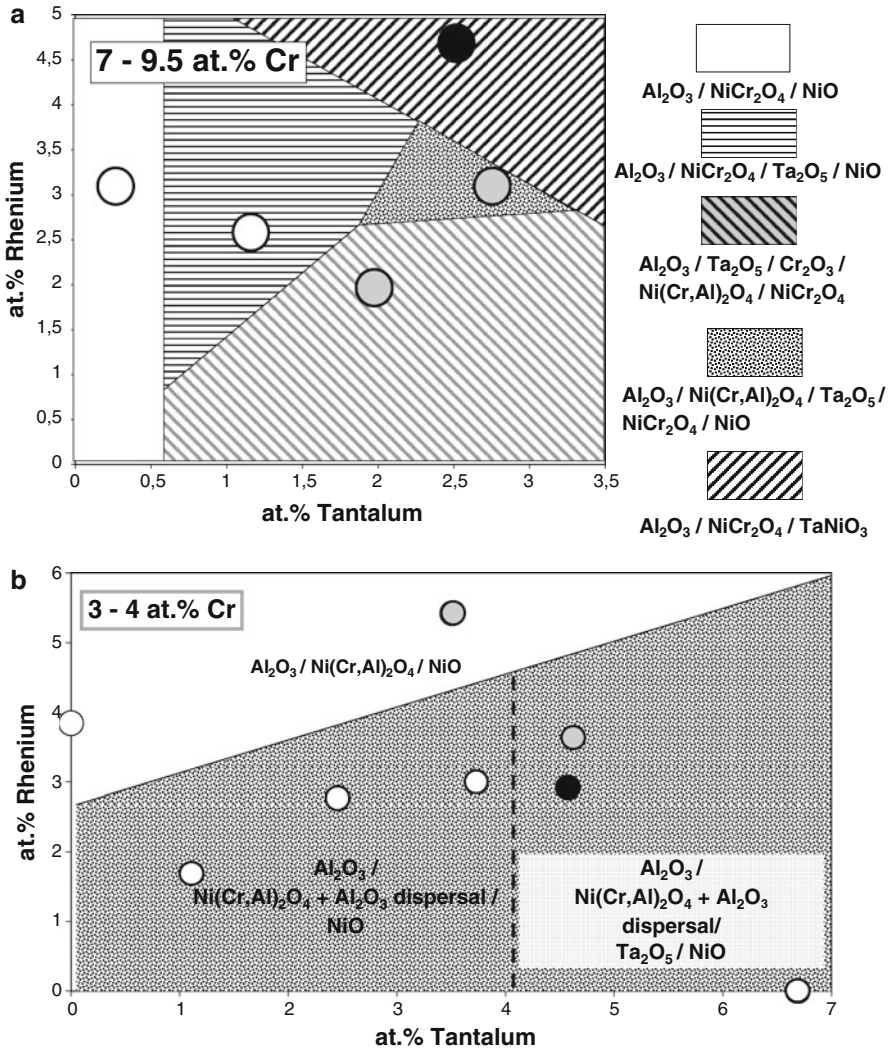
Fig. 10 **a** Oxide map (tentative) for the quinary system Ni–Cr–Al–Ta–Re with 7–9.5 % Cr at 1,000 °C (500 h) showing the respective oxide phases forming on oxidation in air. *Circles* represent alloy compositions, and their shades note the degree of spallation resistance (commented in 10b below). **b** Oxide map (tentative) for Ni–Cr–Al–Ta–Re alloys containing 3–4 % Cr exposed for 500 h at 1,000 °C in air showing the respective oxide phases being formed. *Circles* specify alloy compositions investigated. The *shade* in the circles represents the time regime for stable scale adherence: *open circle* <100 h; *filled circle* 100–500 h; *filled circle* ≥500 h

on thermal expansion could be found. Notably the statement is based on the few existing evaluations. In contrast a trend to low k_p rate constants at low thermal expansions is noticeable according to the best-fit line for 3–4 % Cr alloys (Fig. 12) if approved by the relatively poor statistics. For the 7–9.5 % Cr alloys the diagram may imply that lower k_p rate constants relate to the high Cr containing alloys.
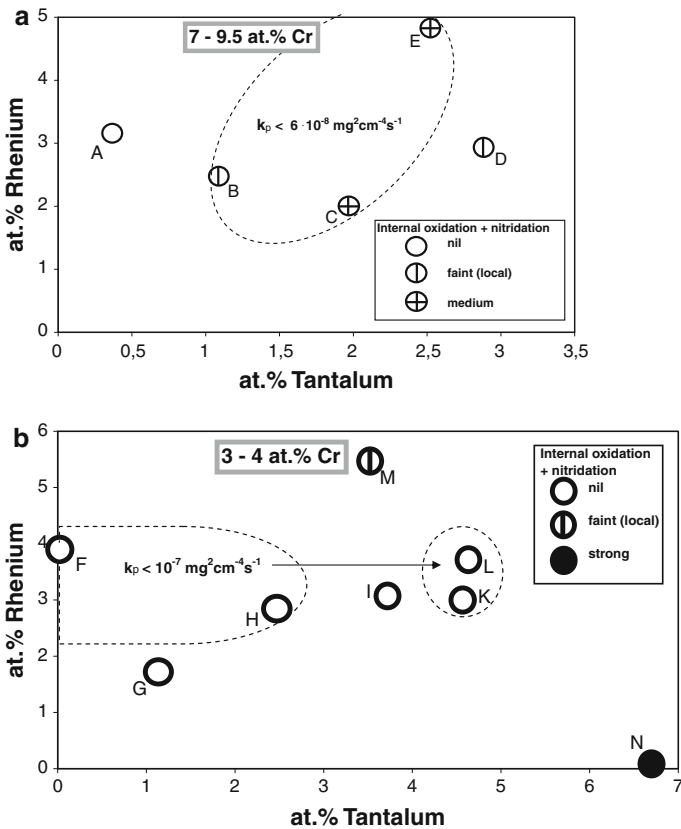
Fig. 11 a Mapping of Re and Ta compositions of Ni–Cr–Al–Ta–Re alloys with 7–9.5 % Cr. Low parabolic weight gain data ($k_p < 10^{-7}$ mg^2 cm^{-4} s^{-1}) of samples excerpted from isothermal tests at 1,000 °C are encircled by a *dashed line*. The susceptibility for internal oxidation is noted. **b** Mapping of Re and Ta compositions of Ni–Cr–Al–Ta–Re alloys with 3–4 % Cr. Low parabolic weight gain data ($k_p < 10^{-7}$ mg^2 cm^{-4} s^{-1}) of alloys obtained from isothermal tests at 1,000 °C are enclosed by *dashed lines*. The tendency for internal attack by O and N is noted

Next the *microstructure at the metal/oxide interface* is considered regarding spallation resistance during cyclic heat exposure. The outstanding characteristics are the length of oxide pegs and convoluted protrusions either slim or irregular-shaped expanding into the metal base. The length of the intrusions is given as a function of the times till onset of scale spallation in Fig. 13. The fit line brings about a reasonable correlation: intrusions between 1 to 2 and 10 μm fit fairly well with time excepting alloy L. Alloy L exhibits very few but extremely long protrusions. They go beyond the data line (see Figs. 7, 13). The reasons for the inferior fit for alloy L may concern: (i) the protrusions along the Me/MeO interface are too infrequent to care for sufficient scale adhesion. (ii) The mushroom-like shape of the protrusions contains prevailing spinel phase which is too weak to stick firmly to the scale and anchor it. In essence no protrusions bring about very early spallation whereas extending protrusions result in longer times without spallation. Obviously the use of
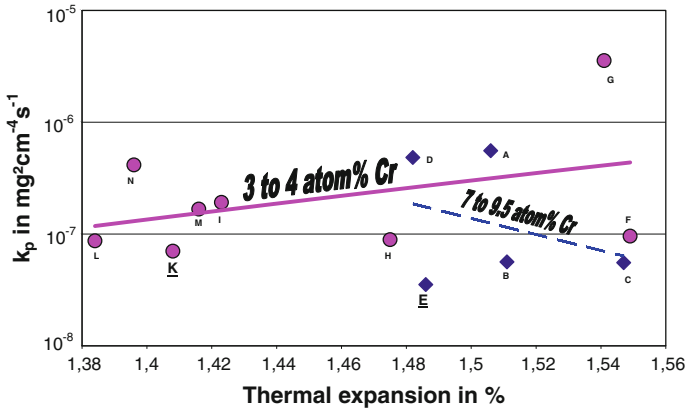
Fig. 12 Parabolic rate constant k_p of the alloys versus their thermal expansion between RT and 1,000 °C. *E* and *K* are most spallation resistant among the low and high Cr alloy series
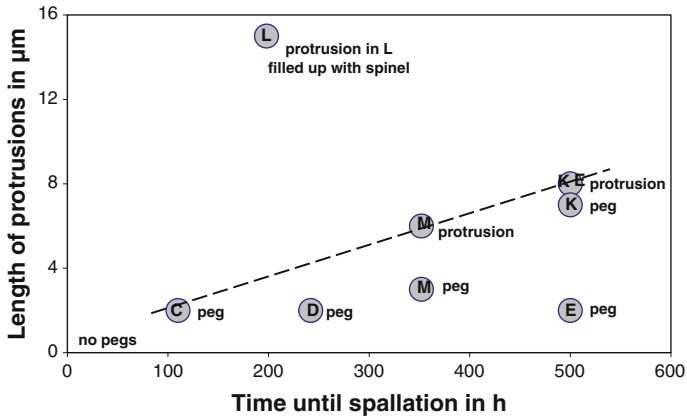

Fig. 13 Duration until onset of scale spallation on thermocyclic testing (22 h at 1000 °C, 2 h at RT and reheat to 1000 °C) versus length of protrusions at Me/MeO interface into the Ni–Cr–Al–Ta–Re substrate. *Letters* within the measured values specify respective alloy designations

oxide protrusions provides some mechanical interlocking of the oxide scales. The keying effect may exceed the stress-related effects of the thermal mismatch at metal/scale interfaces. They undoubtedly exist but are considered to be overshadowed by prevailing mechanical anchoring.

If compared to modern superalloys, however, the spallation resistance of the alloys in this study is still poor. Superalloys are considerably more oxidation resistant. Their scales also have pegs which are very similar to those in this study. The scales on superalloys have a smooth surface in contrast to the scales of this study, and they will never spall after a short time at temperature. The composition of superalloys, however, has a striking feature: e.g. the 2nd generation single-crystal superalloy CMSX-4 contains 0.1 wt% Hf, 3rd generation René N6 has 0.15 wt%

Hf. Both alloys are typically doped with reactive elements that exert a dramatic effect on oxidation. On this note the present cyclic oxidation experiments had the advantage of time. They did not take too long as no reactive elements were involved.

Alloying with reactive element dopants like Hf or Y changes the growth mechanism of α-alumina scales from a mixed Al and O transport to predominantly O transport. Thus the potential transport of transition elements ceases and gives rise to the growth of exclusive alumina [21]. As a result the dimpled outer surface containing numerous protrusions and ridges will be modified to relative smoothness. The grain structure of α-alumina scales will alter from equiaxed to a columnar grain structure; the columnar grains grow longer and coarser with increased oxidation times, whereas fine equiaxed grains at the gas interface only coarsen slightly [22]. Considering that the growth mechanism is via grain-boundary transport, the oxidation of doped alloys must decrease at a much faster rate than is consistent with diffusion-controlled growth, as has been observed [23]. Accordingly sub-parabolic oxidation has also been reported for MCrAlY bondcoats with inverse oxidation rate exponents between 2.5 and 3 at >1,000 °C [24, 25].

The essay given in this chapter will focus on understanding the kinetics observed during isothermal exposure of doped and undoped alloys and on the formation of pegs and protrusions similarly formed below the scale of doped alumina-forming alloys and the undoped Ni-base alloys of this study. The kinetics observed in this study during isothermal exposure fit closely parabolic rate laws which have established after a transition period. Hence they represent the growth of peg-forming scales without the involvement of reactive elements. The adhesion increases slightly versus the grade of interface structuring; it may give an impression of the adhesion strength, which subsists due to exclusive physico-mechanical interlocking of pegs at the interface. It is relatively minor. The bigger portion of adhesion strength, however, which is imparted to alloy/alumina interfaces by doping with reactive elements, is attributed to chemical forces of bonding.

Conclusions

Multi-layered oxide scales grow on the present γ/γ'-phase NiCrAlReTa cast alloys in reactive-element-free condition during cyclic heat exposure in air at 1,000 °C for 500 h. Several scales spall from their substrates after having passed the first cycle, some alloy compositions are more spallation-resistant.

Parabolic oxidation kinetics establishes during 100 h isothermal exposure at 1,000 °C after a heavy weight gain for an initial transition period of ∼10–70 h. Low Cr alloys (3–4 %) have a higher weight gain during transient oxidation than high Cr alloys (8–9.5 %). The low Cr alloys demonstrate lower parabolic rate constants versus a decreasing thermal expansion.

The spallation resistance of the alloys is independent of the lattice spacing of γ-Ni$_{ss}$ in the alloy matrix and of the thermal expansion of the alloys. It will improve according to the following conditions:

- alloying with overcritical amounts of Re and Ta (one single element of the two will not perform well)
- concomitant potential running a low or otherwise super-low parabolic oxidation rate constant
- mechanical interlocking via alumina protrusions at the alloy/alumina subscale interface (the more the longer they are).

References

 1. A. Akhtar, S. Hegde, and R. C. Reed, *Journal of Metals* **58**, 37 (2006).
 2. G. L. Erickson, *The Development and Application of CMSX-10, Superalloys 1996*, eds. R. D. Kissinger et al. (The Minerals, Metals & Materials Society, 1996), p. 35.
 3. B. A. Pint, J. R. DiStefano, and I. G. Wright, *Materials Science & Engineering A* **415**, 255 (2006).
 4. W. S. Walston, K. S. O'Hara, E. W. Ross, T. M. Pollock, and W. H. Murphy, *Rene´ N6: Third Generation Single Crystal Superalloy, Superalloys 1996*, eds. R. D. Kissinger et al. (The Minerals, Metals & Materials Society, 1996), p. 27.
 5. A. Akhtar, M. S. Hook, and R. C. Reed, *Metallurgical & Materials Transactions A* **36**, 3001 (2005).
 6. P. Nash, M. F. Singleton, and J. I. Murray, *Phase Diagrams of Binary Nickel Alloys*, ed. P. Nash (ASM International, Materials Park, OH, 1991).
 7. G. C. Fryburg, C. A. Stearns, and F. J. Kohl, *Journal of the Electrochemical Society* **124**, 1147 (1977).
 8. C. A. Barrett, A statistical analysis of elevated temperature gravimetric cyclic oxidation data of 36 Ni- and Co-base superalloys based on an oxidation attack parameter, *NASA-TM-105934*, NASA LRC, Cleveland, Ohio, December 1992.
 9. A. M. Huntz, J. L. Lebrun, and A. Boumaza, *Oxidation of Metals* **33**, 321 (1990).
10. N. Czech, F. Schmitz, and W. Stamm, *Surface & Coatings Technology* **68–69**, 17 (1994).
11. N. Czech and F. Schmitz, *U.S. Patent* 5,599,385 (1997).
12. Md Moniruzzaman, A. Maeda, Y. Murata, and M. Morinaga, *SISJ International* **43**, 386 (2003).
13. B. Gleeson, W. Wang, S. Hayashi, and D. Sordelet, *Materials Science Forum* **461–464**, 213 (2004).
14. N. Dupin, I. Ansara, and B. Sudman, *Calphad* **25**, 279 (2001).
15. K. Fritscher, C. Leyens, and U. Schulz, *Materials Science & Engineering A* **369**, 144 (2004).
16. K. Kawagishi, A. Sato, and H. Harada, *JOM* **60**, 31 (2008).
17. B. Pieraggi, *Oxidation of Metals* **64**, 397 (2005).
18. H. M. Hindam and D. P. Whittle, *Oxidation of Metals* **18**, 245 (1982).
19. M. Frances, M. Vilasi, M. Mansour-Gabr, J. Steinmetz, and P. Steinmetz, *Materials Science & Engineering* **88**, 89 (1987).
20. O. Unal, T. E. Mitchell, and A. H. Heuer, *Journal of the American Ceramic Society* **77**, 984 (1994).
21. B. A. Pint, J. R. Martin, and L. W. Hobbs, *Oxidation of Metals* **39**, 167 (1993).
22. B. A. Pint, J. A. Garrat-Reed, and L. W. Hobbs, *Materials at High Temperatures* **13**, 3 (1995).
23. I. A. Allam, D. P. Whittle, and J. Stringer, *Oxidation of Metals* **12**, 35 (1978).
24. U. Schulz, M. Menzebach, C. Leyens, and Y. Q. Yang, *Surface & Coatings Technology* **146–147**, 117 (2001).
25. R. D. Jackson, M. P. Taylor, H. E. Evans, and X.-H. Li, *Oxidation of Metals* **76**, 259 (2011).